OPEN ACCESS
IOP Publishing

Made open access 7 August 2017
Journal of Physics G: Nuclear and Particle Physics

J. Phys. G: Nucl. Part. Phys. **44** (2017) 044003 (19pp) https://doi.org/10.1088/1361-6471/aa5a24

Development of a sensitive setup for laser spectroscopy studies of very exotic calcium isotopes

R F Garcia Ruiz[1,2,8], C Gorges[3,8], M Bissell[2], K Blaum[4], W Gins[1], H Heylen[1], K Koenig[3], S Kaufmann[3], M Kowalska[5], J Krämer[3], P Lievens[6], S Malbrunot-Ettenauer[5], R Neugart[4], G Neyens[1], W Nörtershäuser[3], D T Yordanov[7] and X F Yang[1]

[1] Instituut voor Kern-en Stralingsfysica, KU Leuven, B-3001 Leuven, Belgium
[2] School of Physics and Astronomy, The University of Manchester, Manchester M13 9PL, United Kingdom
[3] Institut für Kernphysik, TU Darmstadt, D-64289 Darmstadt, Germany
[4] Max-Planck-Institut für Kernphysik, D-69117 Heidelberg, Germany
[5] CERN, European Organization for Nuclear Research, Experimental Physics Department, CH-1211 Geneva 23, Switzerland
[6] Laboratory of Solid State Physics and Magnetism, KU Leuven, B-3001 Leuven, Belgium
[7] Institut de Physique Nucléaire, CNRS/IN2P3, Université Paris-Sud, Université Paris-Saclay, F-91406 Orsay, France

E-mail: ronald.fernando.garcia.ruiz@cern.ch and chgorges@uni-mainz.de

Received 15 November 2016, revised 31 December 2016
Accepted for publication 18 January 2017
Published 22 February 2017

Abstract

An experimental setup for sensitive high-resolution measurements of hyperfine structure spectra of exotic calcium isotopes has been developed and commissioned at the COLLAPS beam line at ISOLDE, CERN. The technique is based on the radioactive detection of decaying isotopes after optical pumping and state selective neutralization (ROC) (Vermeeren *et al* 1992 *Phys. Rev. Lett.* **68** 1679). The improvements and developments necessary to extend the applicability of the experimental technique to calcium isotopes produced at rates as low as few ions s^{-1} are discussed. Numerical calculations of laser-ion interaction and ion-beam simulations were explored to obtain the optimum performance of the experimental setup. Among the implemented features are a multi-step optical pumping region for sensitive measurements of isotopes with hyperfine splitting, a high-voltage platform for adequate control of low-energy ion beams and simultaneous β-detection of neutralized and remaining ions.

[8] Authors to whom any correspondence should be addressed.

The commissioning of the experimental setup, and the first online results on neutron-rich calcium isotopes are presented.

Keywords: nuclear physics, laser spectroscopy, calcium isotopes, hyperfine structure, atomic physics

(Some figures may appear in colour only in the online journal)

1. Introduction

Laser-spectroscopy techniques provide a powerful tool to extract nuclear structure information on the ground state (gs) properties of exotic nuclei [2, 3]. These techniques allow to extract nuclear gs electromagnetic moments, nuclear gs spins and changes in the root mean square charge radii (rms) without nuclear-model dependence [4]. One of the most commonly used high-resolution laser-spectroscopic techniques is based on optical detection of the fluorescence photons from resonantly laser-excited atoms or ions, by overlapping the laser beam with an accelerated atom or ion beam in collinear geometry. By changing the ion velocity, and thereby Doppler tuning the laser frequency in the ion rest frame, transition energies among different ionic hyperfine structure levels can be measured [5]. Although a resolution of the order of the natural linewidth can be reached, the overall sensitivity obtained with optical detection is significantly reduced due to the intrinsic low efficiency associated to photo-detection [6]. Currently, high-sensitivity experimental setups have shown that the applicability of optical detection is typically limited to minimum yields of about 10^3 ions s^{-1} [7].

A research program at the COLLAPS beam line at ISOLDE-CERN is focused on the study of neutron-rich calcium isotopes. By using optical detection techniques, the hyperfine structure spectra and isotope shifts were measured up to ^{52}Ca. From these experimental results, the gs electromagnetic moments of ^{49,51}Ca [8] and changes in the rms charge radii up to ^{52}Ca [9] were determined for the first time. These results challenged the predictions from the available nuclear models and opened new questions in our understanding of neutron-rich nuclei [9]. Nuclear theory has highlighted the major challenges that remain in our understanding of the evolution of nuclear sizes [10, 11], and the need of extending these experiments further away from stability. Of particular interest is the charge radius of the suggested doubly magic isotope ^{54}Ca [12, 13].

With production yields of less than $\sim$100 ions s^{-1} and $\sim$10 ions s^{-1} for ^{53}Ca and ^{54}Ca, respectively, these isotopes are beyond the limits of optical detection techniques. For the particular case of calcium isotopes, a higher sensitivity can be achieved using alternative schemes based on particle detection [14–18], previously demonstrated at ISOLDE a few decades ago with the study of ^{50}Ca ($\sim 10^5$ ions s^{-1}) [1] and Sr isotopes [19–21]. This work presents some of the technical developments carried out to reach the necessary sensitivity [18] to allow the study of calcium isotopes produced at rates as low as 1 ion s^{-1}.

The experimental method and numerical calculation of the optical pumping process are presented in section 2. A detailed explanation of the beam line and the ion-beam optics simulations used to guide the design of the beam line components follows in section 3. Finally, the commissioning of the beam line and first experimental tests are discussed.

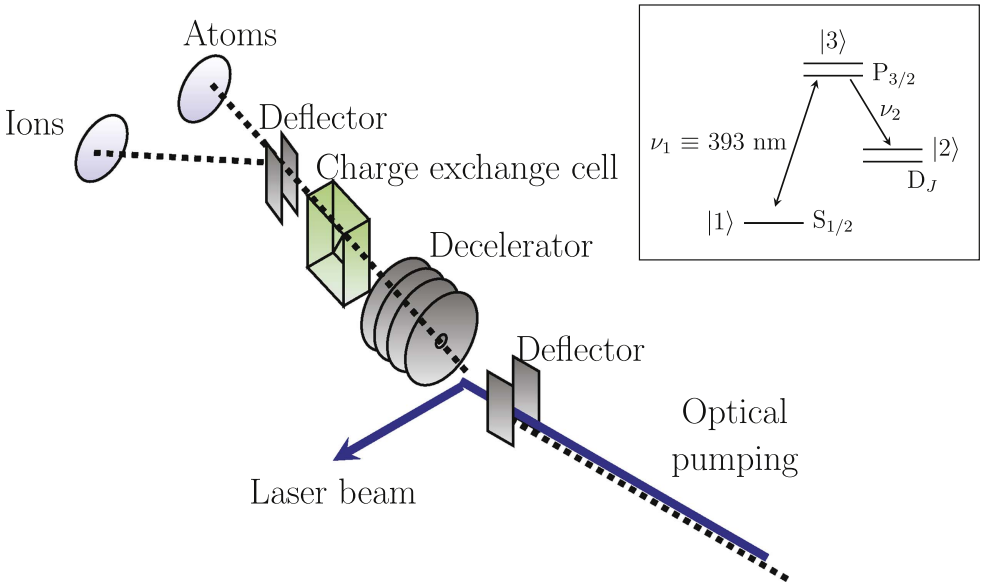

Figure 1. Layout of the experimental scheme. The method covers three main steps; *optical pumping, state-selective charge exchange* and *radioactive detection of atoms/ions*. In the inset the optical pumping scheme used for Ca^{+} is shown. A laser beam with frequency ν_1 is used to resonantly excite the gs states to the $P_{3/2}$ states, which subsequently populates the metastable D_J states by spontaneous emission of a photon at frequency ν_2.

2. Experimental method

A layout of the experimental scheme is shown in figure 1. It consists of three main processes; *optical pumping, state-selective charge exchange*, and *radioactive detection*. First, the ions in the gs are resonantly excited to a short-lived excited state and the subsequent spontaneous decay populates a low-lying metastable state. An example of the level scheme for a calcium ion is shown in the inset of figure 1. An efficient population of the metastable state is achieved by superimposing the laser and the ion beam in collinear geometry along an optical pumping region. Afterwards, the ions are deflected from the laser beam and decelerated prior to the charge exchange cell (CEC). Here, they are neutralized when passing through sodium vapor. The neutralization probability is state selective and the deceleration voltage is chosen to maximize the difference of the neutralization cross sections between the $S_{1/2}$ gs and the metastable D_J states (see below). Finally, an electric field is applied to separate the ions and generated atoms and detect them simultaneously on two separate detectors. Since the neutralization probability in the CEC is significantly different between the $S_{1/2}$ gs and the metastable D_J states, the resonant interaction between the laser and the ions in the first step can be observed as a change in the atom-to-ion ratio as a function of the Doppler-shifted frequency. As such a resonant process only occurs when the applied frequency ν exactly matches the energy difference between hyperfine states of different fine structure levels, this technique provides a sensitive method to measure the hyperfine spectra of ^{53,54}Ca . As the direct detection of the ions and atoms of interest can be compromised by overwhelming isobaric contamination, the detection of charged particles emitted by the radioactive isotopes can be used to suppress stable contaminants. Moreover, the characteristics of the respective

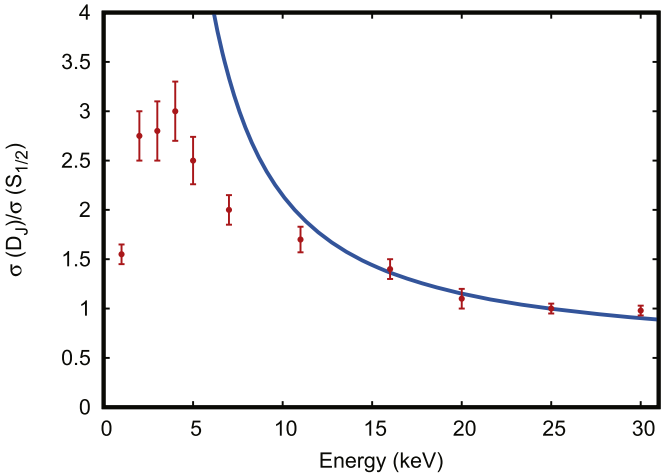

Figure 2. Ratio of neutralization cross sections between the metastable, 3 d^2D_J, and ground state, $4s^2\ S_{1/2}$, for a Ca^+ ion in the reaction $Ca^+ + Na$. Experimental values are taken from [23]. The continuous blue line shows the calculated values using the approach of Rapp and Francis [22] with a normalization factor of 0.5 (see text for more details).

radioactive decays offer the means to suppress other radioactive contaminants. E.g., half-lifes and Q-values of the beta-decay of ^{53,54}Ca are significantly shorter or higher, respectively, than their isobaric contaminants. Hence, detecting the beta-decay and gating on the lifetime and/or the beta energy provides a much clearer signature of the isotope of ^{53,54}Ca than a direct measurement of the ion and atom beam intensities.

2.1. Charge exchange process

The sensitivity of the technique is based on the difference between the neutralization cross sections of the metastable and gs. The neutralization process for a Ca^+ beam passing through a vapor of Na atoms can be expressed as

$$Ca^+ + Na \rightarrow Ca + Na^+ + \Delta E, \tag{1}$$

where ΔE is the so called energy defect [22] given by the difference between the ionization potentials of Ca and Na, which are respectively 6.11 eV and 5.14 eV from the gs. The neutralization cross section of this process depends on the initial ionic state and velocity of the incoming ion [23]. If both Ca^+ and Na are initially in the gs, the neutralization process is considered non-resonant ($\Delta E = 0.97$ eV). However, if Ca^+ is initially in the low-lying metastable states D_J at about 1.7 eV above the gs, a quasi-resonant neutralization process is expected, as reaction channels to excited states in Ca (atom) with $\Delta E \sim 0$ eV can be accessed. The semi-classical approximation introduced by Rapp and Francis [22, 24] is commonly used to describe this charge-exchange process as a function of the impact velocity.

Due to the various approximations used in the theory of Rapp and Francis [22], the derived expressions are not expected to predict the absolute value of the experimental cross sections, but can be used to predict global dependence on the impact velocity and ionic state [23]. The experimental and calculated neutralization cross section ratio between the metastable and gs as a function of the beam energy are shown in figure 2. Although the experimental absolute values are not well reproduced by the theory, the calculated values predict a

rapid increase of the neutralization cross sections at low energies. The global behavior and the order of magnitude is in good agreement at energies above 10 keV, but a normalization factor of 0.5 needs to be included to reproduce the absolute experimental values.

At low energy, the calculated values for the gs cross section tends to decrease towards zero rapidly. Consequently, the cross section ratio $\sigma(D_J)/\sigma(S_{1/2})$ diverges at low energy, contrary to the experimental observation which exhibits a maximum around 4 keV and decrease at lower energies [23].

2.2. Optical pumping

The applicability of the experimental method is restricted to the existence of a low-lying metastable state that can be optically pumped from the gs. Moreover, a near-resonant charge-exchange reaction is required only for one of these states. Such atomic schemes are commonly found in alkaline-earth ions such as Ca, Sr, Ba and Ra. An illustration of the optical pumping process for a calcium ion (Ca^+) is shown in the inset of figure 1. The ions, initially in the $4s\,^2S_{1/2}$ gs, interact with a laser beam, and are resonantly excited to the $4p\,^2P_{3/2}$ states. Subsequent spontaneous emission populates the metastable $3d\,^2D_J$ states[9].

A rate equation model can be used to quantify the evolution of the population during the optical pumping process for a three level system with a gs $|1\rangle$, a meta-stable state $|2\rangle$, and an excited level $|3\rangle$ (figure 1), with population densities N_1, N_2, and N_3, respectively. Spontaneous and induced emission are allowed from the excited state to the gs, as well as spontaneous decay to the meta-stable state (the process that is responsible for population transfer into this level). If the frequency of the external laser field, ν, takes values around the energy difference between the states $|3\rangle$ and $|1\rangle$, ν_{13}, resonant excitation from the gs to the excited state occurs. Thus, the evolution of the population for the different states can be expressed as [27]

$$\begin{aligned}
\frac{dN_3}{dt} &= -(A_{31}+A_{32})N_3 - \rho(\nu_{13})B_{31}(\nu-\nu_{13})N_3 + \rho(\nu_{13})B_{13}(\nu-\nu_{13})N_1,\\
\frac{dN_2}{dt} &= A_{32}N_3,\\
\frac{dN_1}{dt} &= A_{31}N_3 - \rho(\nu_{13})B_{13}(\nu-\nu_{13})N_1 + \rho(\nu_{13})B_{31}(\nu-\nu_{13})N_3,
\end{aligned} \tag{2}$$

with A_{if} and B_{if} the Einstein's coefficients introduced to account for the different processes of spontaneous emission (A_{31}, A_{32}), absorption ($B_{13}(\nu-\nu_{13})$) and stimulated emission ($B_{31}(\nu-\nu_{13})$). The coefficients $B_{if}(\nu-\nu_{if})$ are assumed to have Lorentzian profiles. The spontaneous emission coefficients, A_{if}, between an initial state i and a final state f are characterized by their hyperfine quantum numbers I, J, F, M [28].

For an ion exposed to an electromagnetic field with spectral energy density $\rho(\nu)$, the probability per unit time of absorbing photons, transferring the ion from the state $|i\rangle$ to a final state $|f\rangle$, is given by $\rho(\nu)B_{if}(\nu-\nu_{if})$. Only absorption from the gs to the excited state is considered by assuming an external field with frequency values, ν_{13}, around the energy difference between the states $|3\rangle$ and $|1\rangle$, therefore $\rho(\nu_{23})B_{23}(\nu-\nu_{23}) \sim 0$. Both spontaneous and induced emission are allowed from the excited state to the gs.

The population of the different states involved in the optical pumping process can be calculated by numerically solving the set of coupled differential equations in (2). The final

[9] The $3d\,^2D_J$ states in Ca^+ have a lifetime of about 1.2 s [25]. The branching ratios from the $4p^2P_{3/2}$ states into the $4s\,^2S_{1/2}$ and $3d\,^2D_J$ states are about 0.93 and 0.07 [26], respectively.

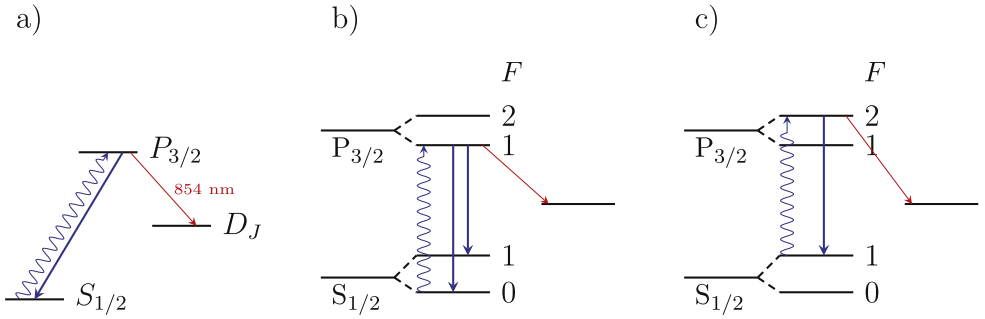

Figure 3. A laser field is used to excite the ion from the ground state, $S_{1/2}$, to the excited state, $P_{3/2}$. The metastable states D_J are populated by spontaneous emission from the excited state. (a) Level scheme of a Ca^+ ion with nuclear spin, $I = 0$. (b) Level scheme of a Ca^+ ion with nuclear spin, $I = 1/2$. When the laser is on resonance with the component $F = 0 \rightarrow F' = 1$, the spontaneous emission spreads the population into the metastable states D_J and the gs components $F = 0$, 1. (c) If the laser is on resonance with $F = 1 \rightarrow F' = 2$, the $F' = 2$ level can not decay to the $F = 0$ ground state. Therefore, the initial population of $F = 1$ can be completely transferred into the metastable states.

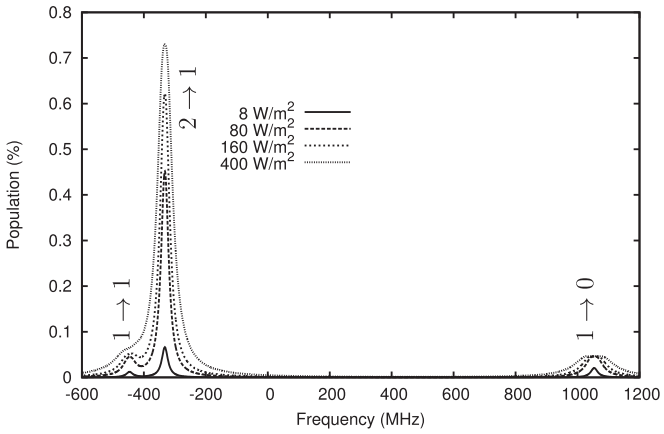

Figure 4. Population of the metastable state as a function of the Doppler-tuned laser frequency with respect to the transition frequency of the line center of gravity. Ions at 30 keV interact on a flight path of 2 m length. The population is calculated for different laser power densities in a single-step optical pumping of ^{53}Ca ($I = 1/2$) (see text for more details).

population of each state can be obtained from the sum of the populations of the different hyperfine levels after a given laser-ion interaction time.

2.2.1. Single-step excitation. For isotopes with nuclear spin $I = 0$, approximately 100% of the ions can be transferred to the metastable state, as these ions do not have a hyperfine structure. Therefore, the pumping efficiency depends mainly on the laser power density and the ion-laser interaction time, which is given by the length of the optical pumping region (see figure 1).

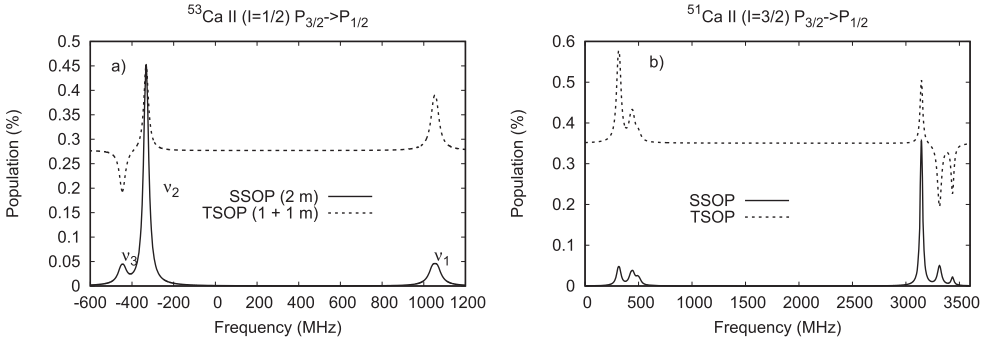

Figure 5. Population of the metastable state for single-step optical pumping (SSOP) and two-step optical pumping (TSOP). A Ca^+ beam at 30 keV is assumed to interact with a laser beam along an optical pumping region of 2 m length. For the TSOP process, the first region of 1 m was used to scan the frequency, and the second step was fixed at frequency of the strongest peak. Calculated populations are shown for (a) ^{53}Ca ($I = 1/2$) and (b) ^{51}Ca ($I = 3/2$). Using the TSOP scheme, all hyperfine transitions can be observed with a similar signal-to-background ratio.

A high pumping efficiency can be reached either by increasing the length of the pumping zone (interaction time) or by increasing the laser power. In practice, laser powers up to a few mW mm^{-2} can be obtained for the 393 nm wavelength used to excite Ca^+. However, as shown in figure 4, high laser power densities can cause significant power broadening. For the final design, an optical pumping region of about 2 m length was chosen as an optimum compromise given the space and laser power constraints. A laser power density of about 0.2 mW mm^{-2} applied to an ion beam of 30 keV kinetic energy, results in about 90% of pumping efficiency into the meta-stable state for ions with nuclear spin $I = 0$.

For ions with nuclear spin $I \neq 0$, the pumping efficiency is strongly affected by trapping the population into different hyperfine components of the states involved in the pumping process. A scheme for a laser field interacting with a Ca^+ with nuclear spin, $I \neq 0$, is shown in figures 3(b), (c). The population of the metastable state can be reduced due to trapping into other hyperfine components of the gs (figure 3(b)).

Figure 4 shows the population of the metastable state after single-step optical pumping (SSOP), i.e. resonant excitation of a ^{53}Ca ion with only one laser field, assuming nuclear spin $I = 1/2$. The population is calculated for different laser power densities and using 6 μs interaction time, which is equivalent to an ion beam at 30 keV passing through an interaction region of 2 m length. When the laser is at resonance with the $F' = 1$ excited hyperfine level, by excitation from the $F = 0$ or from the $F = 1$ gs level, part of the spontaneous decay depopulates into the non-excited gs hyperfine level (see figure 3(b)). This fraction of ions is lost for the remaining of the optical pumping process, which proceeds through the spontaneous decay from excited state hyperfine levels to the metastable D state. Thus, in figure 4 only one hyperfine transition efficiently pumps the ions into the metastable states, namely $F = 1 \rightarrow F' = 2$ transition, which forms essentially a two-level system since the $F' = 2$ level can not decay to the $F = 0$ gs (see figure 3(c)). Therefore, only one of the three hyperfine transitions has a significantly large amplitude to be detected in the experiment, and thus no information about nuclear moments nor radii can be extracted.

2.2.2. Two-step excitation. As discussed above, two of the three hyperfine transitions are weakly observed at best using a single laser field. In order to gain similar signal strength for

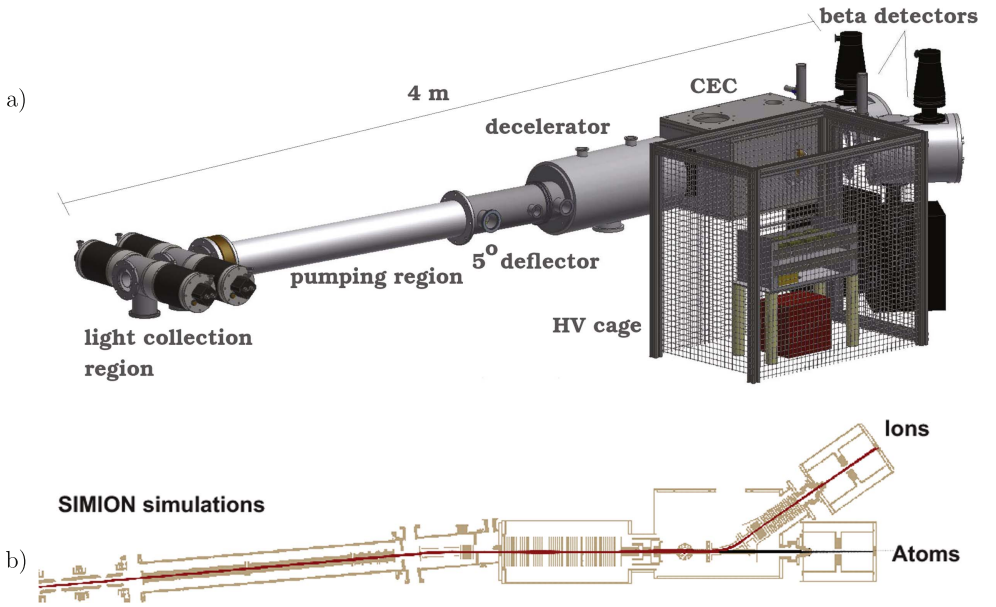

Figure 6. Complete design of the new ROC setup. (a) Technical design drawing created by using Autodesk Inventor. (b) Particle trajectories simulated with SIMION: ions (red) and neutralized particles (black).

all three hyperfine components, two laser fields of different frequency can be applied for simultaneous pumping from different hfs components. This two-step optical pumping (TSOP) can be used to minimize population transfer into non-interacting hyperfine levels [20, 29, 30].

A comparison of different numerical calculations for both SSOP and TSOP are shown in figure 5. In TSOP it is assumed that the laser frequency in the first section of the optical pumping region can be varied, while it is fixed at the resonance position of the closed $F = I + 1/2 \rightarrow F' = I + 3/2$ transition in the second section.

If the frequency seen by the ion in the first step does not match the resonance condition, no change of population occurs. In this case, only in the second section the excitation of the state $F = I + 1/2$ occurs and pumping into the meta-stable states takes place. This signal establishes the base line shown in figure 5 for the TSOP calculations. Then, when the first region is scanned across the hyperfine resonances, e.g. around the resonance frequency ν_3 ($F = I + 1/2 \rightarrow F' = I - 3/2$), the state $F = I + 1/2$ is depopulated partially into the meta-stable state, but mostly to the state $F = I - 1/2$. As the state $F = I - 1/2$ is not interacting with the laser in the second region, the net population of the meta-stable state is reduced significantly. This causes a decrease in the meta-stable state population, observed as a dip with respect to the base line at the frequency ν_3, as shown in figure 5. However, if the first region is scanned around ν_1 ($F = I - 1/2 \rightarrow F' = I + 1/2$), the state $F = I - 1/2$ is completely depopulated transferring some of the ions to the metastable states D_J, and partially into the gs component $F = I + 1/2$, but the population in this level can be transferred to the metastable state when passing the second region. Therefore, an increase of population with respect to the base line is observed (see figure 5). Similarly, if the first region is scanned around the frequency, ν_2, the population of the metastable state is enhanced along both optical pumping regions. The calculated population for $I = 3/2$ is shown in figure 5(b).

Technically, the TSOP process is achieved with a single laser field along the optical pumping region, which is divided in two regions at different potential (more details below). In the first section the potential is changed to Doppler-tune the laser frequency, while in the second pumping section the potential is fixed to always obtain the resonance condition of the closed two-level system, $F = I + 1/2 \rightarrow F' = I + 3/2$. Experimentally, these changes in the population of the metastable states are observed as a change in the atom to ion ratio.

3. Ion beam optics

An overview of the design to realize the ROC method is shown in figure 6. The total length of the newly installed setup is ∼4 m. The ion beam interacts with a laser beam along an optical pumping zone of 2 m length. The length of the interaction region was chosen to obtain >90% pumping efficiency for transferring the gs population into metastable states for ions with nuclear spin $I = 0$. The introduction of multiple potentials along the pumping region allows the pumping of different hyperfine components, enhancing the signal of weakly populated hfs transitions in odd-isotopes by more than one order of magnitude, depending on the nuclear spin and the number of pumping steps, as explained above.

After optical pumping into the metastable states, the ion beam is separated from the laser beam by a 5° electrostatic deflector, and directed into an electrostatic decelerator. The laser beam is removed from the beam line by a metal mirror placed after the electrostatic deflector. It is necessary to prevent possible laser light impinging on the implantation point and affecting the photomultipliers in the tape station. The deflection is achieved by a couple of cylindrical lenses of long curvature radius (∼2 m), preserving the plane of motion for the ion beam, and minimizing undesired focusing effects.

After deceleration, the ion beam passes through a CEC filled with Na vapor. Atoms and remaining ions are separated with electrostatic plates and independent counting of neutralized and non-neutralized particles is performed at the end of the beam line by their radioactive decay using two independent beta-detection chambers, each including a tape station. Simultaneous detection of both atoms and ions after the deceleration and the subsequent neutralization processes is achieved by introducing multiple ion beam optics components floating at the CEC potential (26 kV). A detailed explanation of the beam line components is presented in the following sections.

3.1. Beam line components

3.1.1. Multi-step optical pumping and fluorescence detection. The optical pumping region for the current design is shown in figure 6. The ion beam is superimposed with the laser beam along a pumping zone divided in four segments with lengths of 40 cm, 60 cm, and two of 50 cm. The first segment (not shown in the figure) corresponds to a pumping tube of 40 cm length. A light collection region is installed along the second pumping segment for monitoring the resonant fluorescence signal during the experiments. This light collection region is the same as the one used in the previous optical hfs experiments on calcium and potassium isotopes [5, 7, 8, 31].

In the experiment, the hfs spectrum of a particular isotope is scanned by changing the potential of the optical pumping region. Regardless of the voltage applied to the optical pumping zone (±5 kV), the ion beam transmission up to the end of the beam line should remain unaltered. To avoid abrupt changes between the optical pumping zone and the ground potentials, a four-step accelerator (decelerator) set connects the beginning (end) of the optical pumping region with the rest of the beam line. For ions with nuclear spin $I = 0$, all pumping

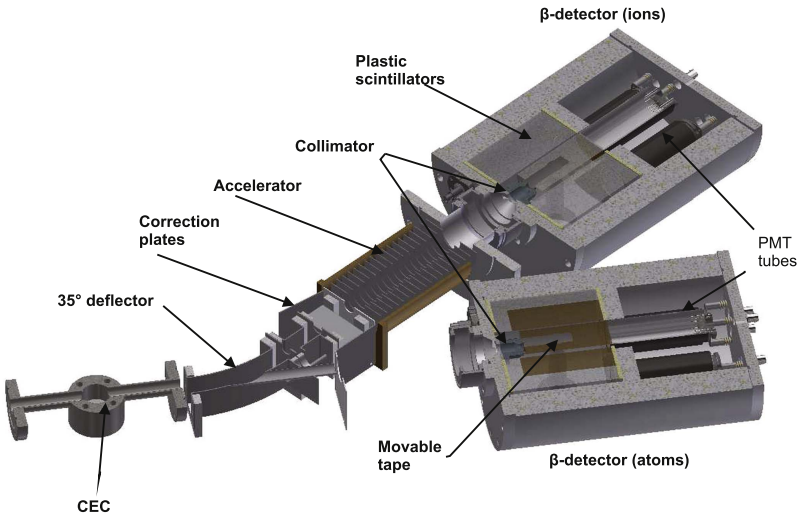

Figure 7. CAD design for the ion beam optics after the CEC. Independent high efficiency β-detection was implemented for atoms and ions. Details for the β-detector chambers are given in section 3.1.4.

segments are fixed at the same potential, and the Doppler-tuning voltage is applied to the whole optical pumping region. For odd ions ($I \neq 0$), independent potentials can be applied to each pumping segment for multi-step optical pumping (see section 2.2). When the TSOP scheme is used, the last two sections are set to a constant voltage corresponding to the most intense resonance peak in the hyperfine spectrum. Scanning across the full hyperfine structure is then performed by changing the voltage on the first and second section (both at the same potential).

3.1.2. Decelerator and focus control of atom/ion beam. As the ratio of the neutralization cross section between the metastable state and the gs is maximum at 4 keV, the initial ion energy (30 keV) should be reduced by about 90% of its initial value, i.e., the potential of the CEC section is fixed at 26 kV. This deceleration has the strongest impact on the overall beam transport. Beam divergences, and undesired focusing can be easily introduced during the deceleration. Since maximum beam transport efficiency is required, the possibility to control the focus of the decelerated beam is essential, as both ions and atoms must be separated and implanted simultaneously on two independent tapes of 10 mm width. Large background levels can be introduced if radioactive contamination is implanted around the β-detectors [1].

In order to minimize the focusing effects during the deceleration process, the ion beam is passed through an array of 52 equidistant disks of 1.5 mm thickness. Each disk has an outer diameter of 14 cm, and a concentric hole of 4 cm diameter. The CAD design and the ion (atom) beam trajectories optimized with the ion-trajectory software SIMION are shown in figure 6(b). The decelerator system is the same as used in past experiments [1], but an adjustable slope for the deceleration potential, and an einzel lens between the decelerator and the CEC were implemented to control the focus for both atom and ion beams [32]. The focus

of the atom beam can be controlled by changing the focus of the ion beam before the neutralization in the CEC.

3.1.3. Simultaneous detection of β-decay of atoms and ions. After deceleration, the low energy ion beam is passed trough the CEC. Afterwards, the ions are separated from the neutralized particles by a pair of electrostatic cylindrical plates as shown in figure 7. Horizontal and vertical correction plates were added to control the position of the implantation point of the remaining ions. The atoms follow a straight path towards the beta-detection station, located at 53 cm from the end of the CEC, and the ions are deflected 35° towards a second tape station at 68 cm from the end of the CEC. Because both β-detection stations are at ground potential, a post-accelerator can be used to gradually decrease the potential seen by the ion beam, from the CEC potential (26 kV) down to the ground potential (0 kV). This re-acceleration process is accomplished by a set of 18 equidistant disks connected by resistors of equal value. As the tape station is close to the end of the accelerator, no further focus control was needed.

A direct detection of the number of atoms and ions is sensitive to isobaric contamination present in the ion beam. However, a selective measurement of the number of particles for the ion of interest can be obtained by counting the β-particles emitted from the beta-decaying nuclei. β detection removes completely the background associated with stable contaminants. The background emanating from radioactive isobars (mainly Ti isotopes) can also be reduced if additional energy and half-life discrimination is implemented.

3.1.4. β-decay setups. Each β-detector chamber is composed of two concentric cylindrical scintillators with inner and outer radius of 50 mm and 190 mm respectively. The axis of each cylinder coincides with the beam direction. The signal from the inner detector is read out by one photomultiplier (PMT), while that of the outer detector is read out by 4 PMTs. A movable tape perpendicular to the beam direction can circulate through the center of both cylinders. This configuration allows for a geometrical efficiency of $\sim 4\pi$ at the implantation point. Particle coincidences between the inner and outer cylinder are used to discriminate the β-particles from other sources of radiation, e.g., γ-radiation. The intrinsic β-detection efficiency of this setup is expected to be $>80\%$. The thickness of the outer detector was chosen to stop all β-particles emitted with energies below 12 MeV, which is close to the highest beta energy expected for ^{54}Ca. A full energy reconstruction of the β-particles could be obtained by adding the signals of all 5 PMTs, which collect the light from the scintillators.

The β-particles emitted from the radioactive isotopes implanted on the tape are recorded on the site of implantation point. After few hundreds of milliseconds[10], the contaminated part of the tape is removed, and a clean section of the tape is placed in front of the beam path at the center of the β-detectors. Each collection time is synchronized with a change of the ion velocity (Doppler-tuning of the laser frequency). A collimator of 10 mm aperture is placed at the entrance of each chamber to prevent the implantation of the radioactive contamination next to the tape.

4. First experimental results

The design and dimensions of the beam-line components were chosen based on numerical simulations of the laser-ion interaction and ion optics explained in the previous sections.

[10] For ^{54}Ca ($T_{1/2} = 86(7)$ ms) the detection time is around 400 ms.

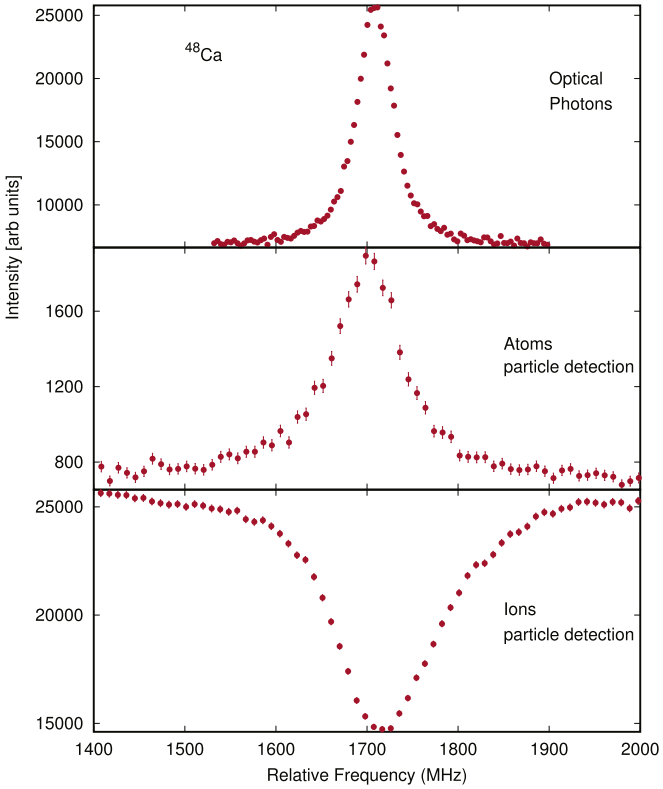

Figure 8. Example of measured spectra of ^{48}Ca. Fluorescence photons (top) are compared with the signal of atoms, neutralized in the CE process (middle), and ions, non-neutralized in the CE process (bottom). All signals are plotted as a function of the laser frequency in the ion rest frame. The four segments of the optical pumping region were fixed at the same potential and used as one Doppler-tuning region.

The first tests were performed by using the GPS target station at ISOLDE. A beam of $^{48}Ca^{+}$ was extracted using the RILIS ion source, accelerated to 30 keV, mass separated and sent to the COLLAPS beam line.

Some of the modifications and improvements implemented in the new ROC setup were expected to improve the overall ion beam transmission. Three main concerns were explored through the first ion beam test: firstly, the ability to reduce the energy from 30 to 4 keV while preserving the transmission at the end of the beam line; secondly, the focus control of the ion beam after the deceleration process and an effective control of the ion beam optics on the top of the HV platform at 26 kV; finally, the dependence of the overall ion beam transmission on the Doppler-tuning voltage applied to the optical pumping region.

The ability to localize the ion focus on the implantation point is important to reduce the risk of implanting radioactive contamination next to the tape. The focus control of the ion beam after deceleration was studied and maximum transmission points were found in agreement with the expectations from the ion optics simulations.

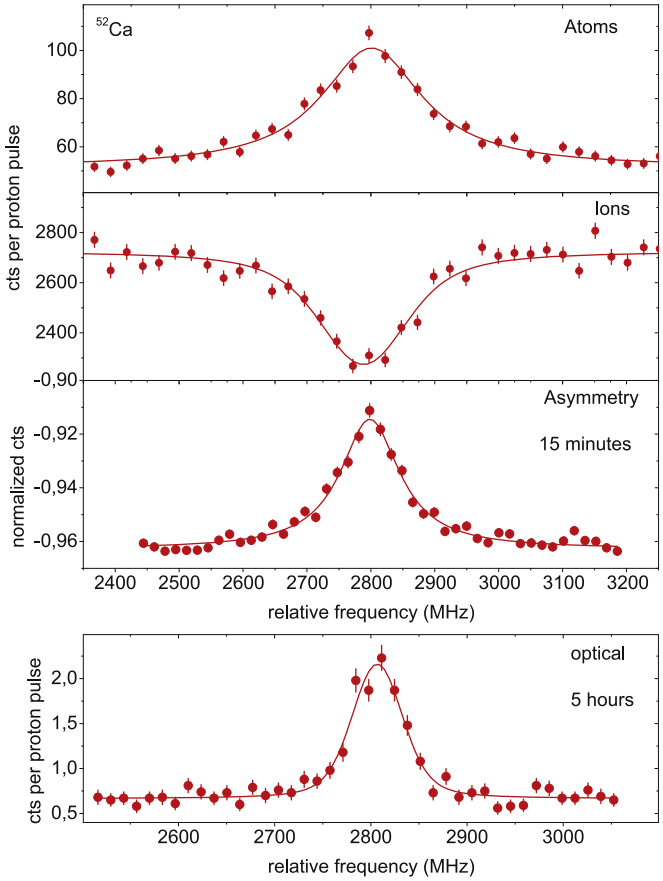

Figure 9. Example of some measured spectra for ^{52}Ca fitted with Voigt profiles. For the atom and ion signal the β-particles per proton pulse in both chambers were measured as a function of the Doppler-tuning voltage applied to the optical pumping region and converted to the respective frequency in the ion rest frame. The top figure shows the spectrum obtained by recording the yield of neutralized atoms. The spectrum recorded simultaneously detecting the non-neutralized ions is shown in the second panel. In the third panel the calculated asymmetry signal (equation (3)) is depicted. In the bottom panel the optical signal taken from [9] is shown. For comparison, the measurement time is indicated in the two lowest panels.

4.1. Optical detection versus state-selective neutralization

The comparison between optical and ROC spectra was performed first with a stable $^{48}Ca^{+}$ beam. The laser frequency was fixed around the 393 nm $4s\ ^2S_{1/2} \rightarrow 4p\ ^2P_{3/2}$ ionic transition of Ca^{+}. To benchmark the ROC measurements, fluorescence photons were detected by using the light collection region installed as part of the optical pumping region (second step). An example of an optical spectrum and corresponding spectra of ions and neutralized atoms as a function of the scanning frequency for stable ^{48}Ca is shown in figure 8. The Doppler-tuning voltage applied to the pumping region was converted to the laser frequency in the ion rest frame.

The ion signals after state-selective optical pumping of the stable isotopes were obtained using a Faraday cup replacing the tape station and converting the ion current into a counting

Table 1. Isotope shift and nuclear charge radii of ^{52}Ca with the ROC method compared to literature values given by [9]. The first bracket shows the statistical uncertainty, and the second bracket the systematic uncertainty associated to the factors K and M, which are related to voltage uncertainties. See text for more details about the systematic shift observed for the ion signal.

$\delta\nu_{\mathrm{IS}}^{52,48}$ (MHz)	$\delta\langle r^2\rangle^{52,48}$ (fm^2)	
512.7(16)[68]	0.531(5)[15]	[9]
510.5(27)[55]	0.530(9)[43]	ROC—atom signal
502.8(28)[55]	0.557(9)[44]	ROC—ion signal

rate. Behind the CEC chamber, a conversion plate was placed in the beam path of the neutralized particles. Atoms hitting the conversion plate produce electrons that are guided to and counted by a channel electron multiplier (channeltron) to obtain the ROC signals of stable isotopes. These state-selective optical pumping signals were taken with laser powers of about 25 mW and laser beam spots of about 10 mm diameter ($\sim$0.3 mW mm^{-2}). Optical signals where recorded at low laser power of about 1 mW to reduce the stray-light background on the photo-multipliers. It can be seen in figures 8 and 9 that the $\sim$130 MHz width of the ROC-peaks is more than twice as large as the $\sim$60 MHz width of the peaks observed with optical detection, which is much less power broadened. The natural linewidth of this transition is about 23 MHz.

The peak positions obtained with the ion detection scheme exhibited a systematic shift of a few MHz with respect to the signal provided by the atoms (see figures 8 and 9). The reason for this shift is still under investigation. The ion beam transmission to the end of the beam line might change with the voltage applied to the pumping zone. It could be the source of the observed shift in the ion signal. As the ions are re-accelerated from the CEC potential (26 keV) up to the ground potential, a strong focus is induced near to the implantation point. The atom signal would not be so sensitive as atoms are unaffected by the strong field.

4.2. First ROC signals for exotic ^{51,52}Ca

The isotopes ^{51,52}Ca were selected to perform the first ROC measurements. Figure 9 shows the number of β-particles detected in both detector chambers, atoms and ions, plotted as a function of the laser frequency in the ion rest frame. For the radioactive isotopes, ^{51,52}Ca, the measured signals can fluctuate due to changes in the ion beam current, caused by, e.g., changes in the proton pulse period, target performance and/or changes in the laser ionization efficiency in the ion source. However, these fluctuations can be removed by taking the normalized difference between the atom and the ion signal (asymmetry), defined as

$$\text{Asymmetry} \equiv \frac{N_{\text{atoms}} - N_{\text{ions}}}{N_{\text{atoms}} + N_{\text{ions}}}. \tag{3}$$

The isotope shift values and the corresponding change in the nuclear charge radius obtained from the neutralized particles (atom signal) are in excellent agreement with our recently published values in [9] (see table 1). However, in the ion signal, a systematic deviation of a few MHz was observed.

Changes in the rms charge radii were obtained from the measured isotope shifts relative to ^{48}Ca, $\delta\nu^{A,48}$, using the standard expression

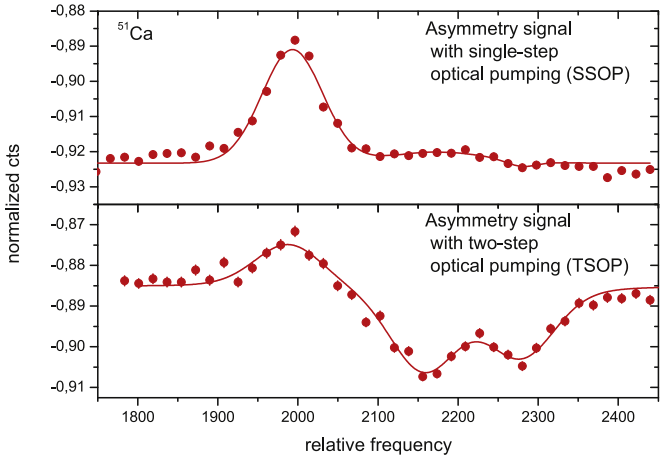

Figure 10. The three peaks with the highest frequencies of the spectrum for ^{51}Ca (having 6 hfs peaks for a $I = 3/2$ isotope, see figure 5). The upper panel shows the asymmetry signal (see equation (3)) using single-step optical pumping, the lower panel shows the signal with TSOP, which allows to observe all 3 hfs transitions from the highest multiplet. The TSOP spectrum was fitted by fixing the hfs parameters $A(^2S_{1/2})$ to the literature value [8]. The observed peaks were fitted to Voigt profiles. A FWHM of about 80 MHz was obtained.

$$\delta\langle r^2\rangle^{A,A'} = \frac{1}{F}\left(\delta\nu^{A,A'} - \frac{m_A - m_{A'}}{m_A \cdot m_{A'}} \cdot K\right). \tag{4}$$

The mass-shift factor, K, and the field-shift factor, F, were derived from a King plot analysis [33], using the isotope shifts measured by optical detection for the stable isotopes $A = 42, 44, 48$.

The remarkable higher sensitivity of the new technique is demonstrated in figure 9 where the counts per proton pulse with ROC are compared to those obtained with the optical detection method. By the particle detection the counts per proton pulse are raised significantly which means a much higher sensitivity and correspondingly a considerably shorter measurement time. The observation of the optical spectrum of ^{52}Ca in [9] took several hours while with the ROC method the peak position can be determined with similar uncertainty after only a few minutes of measurement time.

The importance of multi-step optical pumping for measurements of odd isotopes is shown in figure 10, where the right side of the spectrum of ^{51}Ca is displayed for both SOP and TSOP. These results demonstrate the considerable increase in efficiency achieved with the ROC technique for both even and odd isotopes.

To observe the three hyperfine components of ^{51}Ca, the TSOP method has been applied (see section 2.2). Figure 10 shows the three hyperfine components of the highest energies with the usually used SSOP (top) compared to the TSOP (bottom). In the TSOP spectrum, the three peaks can be clearly seen after about 15 min measurement time, whereas in the SSOP spectrum only the strongest one is visible, as expected from the numerical calculations presented in figure 5.

The atom and ion signals are compared with the normalized signal (asymmetry) in figure 11. As during the TSOP process the laser is constantly resonant with the transition during part of the interaction region, the measured atom and ion signals are very sensitive to

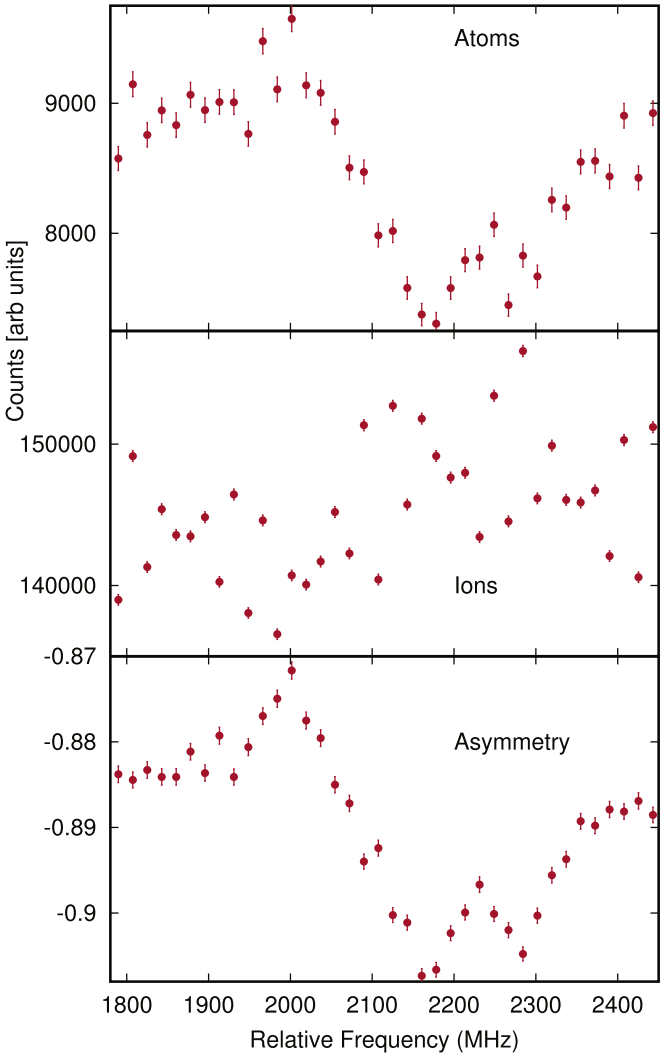

Figure 11. Right multiplet of the spectrum of ^{51}Ca obtained with TSOP: atom signal (upper), ion signal (middle) and asymmetry (lower).

fluctuations of the ion beam current, this is why the full structure can be seen clearly only in the asymmetry signal.

In order to test the TSOP scheme, the higher multiplet of ^{51}Ca was measured. Since the full hfs was not recorded, the $A(^2S_{1/2})$ factor of the gs cannot be extracted. However, by fitting the asymmetry spectrum with the hyperfine parameter of the lower state, $A(^2S_{1/2})$, fixed to the literature value obtained from optical detection [8], the hyperfine parameters $A(^2P_{3/2})$ and $B(^2P_{3/2})$ can be obtained. The values obtained from the ROC measurements with the TSOP method are listed in table 2 together with literature values [8]. The magnetic moment of ^{51}Ca can be calculated by comparing the hyperfine parameter $A_{^{51}\mathrm{Ca}}$ to reference values μ_{ref} and A_{ref} and taking into account the nuclear spins, according to

Table 2. Hyperfine parameter values, magnetic moment and quadrupole moment of ^{51}Ca obtained from the ROC measurements compared to literature values. The literature value of μ extracted from the $A(^2P_{3/2})$ value reported in [8] is shown. The values are in good agreement with the high-precision literature value $\mu = -1.0496(11)\mu_N$ [8] extracted from the $A(^2S_{1/2})$ value (not measured in this work).

$A(^2P_{3/2})$ (MHz)	$B(^2P_{3/2})$ (MHz)	$\mu(\mu_N)$	Q (b)	
−58.15(54)	5.4(18)	−1.050(16)	0.036(12)	[8]
−59.0(15)	5.7(48)	−1.065(28)	0.037(32)	ROC-TSOP

$$\mu_{^{51}\mathrm{Ca}} = A_{^{51}\mathrm{Ca}} \cdot \frac{\mu_{\mathrm{ref}}}{A_{\mathrm{ref}}} \cdot \frac{I_{^{51}\mathrm{Ca}}}{I_{\mathrm{ref}}}. \tag{5}$$

The nucleus ^{43}Ca was used as reference isotope with known $A_{\mathrm{ref}} = -806.40207160(8)$ MHz [34] and $\mu_{\mathrm{ref}} = -1.3173(6)\mu_N$ [35].

The quadrupole moment Q depends on the hyperfine parameter constant B, the electron charge e and the electric field gradient V_{zz} produced by the electrons at the nucleus

$$B = eV_{zz} \cdot Q. \tag{6}$$

The factor $eV_{zz} = 151.3(7)$ MHz/b has been calculated based on relativistic coupled-cluster-theory [36]. The magnetic moment and the quadrupole moment of ^{51}Ca were calculated by using equations (5) and (6). Table 2 compares the values obtained with ROC-TSOP, and literature values. They are in good agreement within uncertainties.

5. Conclusions

With the aim of extending our experimental knowledge of the gs properties of exotic calcium isotopes produced at rates lower than a few hundred ions s^{-1}, a sensitive experimental setup is being developed at the COLLAPS beam line. The technique is based on the radioactive detection of decaying isotopes after optical pumping and state selective neutralization (ROC) [1].

The numerical calculations for the laser-ion interaction and ion beam optics simulations that guided the design of the ion-beam optical elements and beam line components were presented. A laser-ion interaction region of about 2 m length and divided in up to four regions of different potentials was included to allow multiple-step optical pumping to be performed. Additionally, the incorporation of multiple ion beam optic elements floating at the deceleration potential allowed simultaneous detection of β-counts from both atoms and ions.

The experimental setup has been commissioned at the COLLAPS beam line and the first successful experimental tests have been performed. The measurements obtained for the exotic ^{51}Ca and ^{52}Ca isotopes produced at rates lower than 10^3 ions s^{-1} demonstrated the large increase of sensitivity by more than an order of magnitude of the present setup with respect to the previous sensitivity limits achieved with optical [9] and particle detection [1] for calcium isotopes. In only a few minutes time, the statistics acquired for the isotopes ^{51,52}Ca was comparable to those obtained after several hours of measurements with the previously used optical detection scheme [9].

By detecting both, ions and atoms simultaneously, the dependence of the β-count signals with ion beam intensity was significantly reduced. Such normalization was proven to be particularly important when multi-step optical pumping is employed.

Although the current setup has already reached a remarkable sensitivity compared to the results previously obtained with optical detection, several shortcomings were identified during the online experiments. An offline ion source is being developed at the COLLAPS beam line to study the systematic shift observed in the ROC-ion signals, and to improve the transport efficiency in the atom direction. Additionally, developments on the β-detector setup and tape stations are required to reach higher efficiency and long term stability for β-detection. Further background reduction for β-detection is expected by including energy discrimination of β-particles. These improvements are ongoing for the next experimental campaign, which is expected to provide first laser spectroscopy measurements of the very exotic ^{53}Ca and ^{54}Ca isotopes.

Acknowledgments

This work was supported by the IAP-project P7/12, the FWO-Vlaanderen, GOA grant 15/010 from KU Leuven, the BMBF Contracts 05P15RDICA and 05P15RDFN1, the Max-Planck Society, the EU FP7 via ENSAR No. 262010, and the ERC Grant No. 648381 FNPMLS. We would like to thank the ISOLDE technical group for their support and assistance.

References

[1] Vermeeren L *et al* 1992 *Phys. Rev. Lett.* **68** 1679
[2] Cheal B and Flanagan K 2010 *J. Phys. G: Nucl. Part. Phys.* **37** 113101
[3] Blaum K, Dilling J and Nörtershäuser 2013 *Phys. Scr.* **T152** 014017
[4] Campbell P, Moore I and Pearson M 2016 *Prog. Part. Nucl. Phys.* **86** 127–80
[5] Papuga J *et al* 2013 *Phys. Rev.* C **90** 034321
[6] Nörtershäuser W and Geppert C 2014 *Lecture Notes Phys.* **879** 233
[7] Papuga J *et al* 2013 *Phys. Rev. Lett.* **110** 172503
[8] Garcia Ruiz R F *et al* 2015 *Phys. Rev.* C **91** 041304(R)
[9] Garcia Ruiz R F *et al* 2016 *Nat. Phys.* **12** 594
[10] Hagen G *et al* 2016 *Nat. Phys.* **12** 186
[11] Lapoux V *et al* 2016 *Phys. Rev. Lett.* **117** 052501
[12] Wienholtz F *et al* 2013 *Nature* **498** 7454
[13] Steppenbeck D *et al* 2013 *Nature* **502** 207
[14] Silverans R *et al* 1985 *Hyperfine Interact.* **24** 181
[15] Neugart R, Klempt W and Wendt K 1986 *Nucl. Instrum. Methods* B **17** 354
[16] Silverans R, Lievens P and Vermeeren L 1987 *Nucl. Instrum. Methods* B **26** 591
[17] Schulz C *et al* 1991 *J. Phys. B: At. Mol. Opt. Phys.* **24** 4831
[18] Lievens P *et al* 1992 *Nucl. Instrmum. Methods* B **70** 532
[19] Silverans R 1988 *Phys. Rev. Lett.* **60** 2607
[20] Lievens P *et al* 1991 *Phys. Lett.* B **256** 141
[21] Lievens P *et al* 1992 *Phys. Rev.* C **46** 797
[22] Rapp D and Francis J 1962 *J. Chem. Phys.* **37** 2631
[23] Vermeeren L *et al* 1992 *J. Phys. B: At. Mol. Opt. Phys.* **25** 1009
[24] Bruckmeier R, Wunderlich C and Figger H 1995 *Phys. Rev.* A **52** 334
[25] Kreuter A *et al* 2005 *Phys. Rev.* A **71** 032504
[26] Gerritsma R, Kirchmair G, Zähringer F, Benhelm J, Blatt R and Roos C F 2008 *Eur. Phys. J.* D **50** 13–9
[27] Silfvast W 2008 *Laser Fundamentals* 2nd edn (Cambridge: Cambridge University Press)
[28] Foot C 2005 *Atomic Physics* 1st edn (Oxford: Oxford University Press)
[29] Vermeeren L 1990 *Hyperfine Interact.* **61** 1399
[30] Lievens P *et al* 1990 *Hyperfine Interact.* **59** 161
[31] Kreim K *et al* 2014 *Phys. Lett.* B **731** 97

[32] Garcia Ruiz R F 2015 Investigating the possible magicity of $N = 32$, 34 in exotic calcium isotopes using laser spectroscopy methods *PhD Thesis* KU Leuven
[33] King W H 1964 *Proc. R. Soc.* A **280** 430
[34] Arbes F *et al* 1994 *Z. Phys.* D **31** 27
[35] Olschewski L 1972 *Z. Phys.* **249** 205
[36] Sahoo B 2009 *Phys. Rev.* A **80** 012515